ARTICLES
PUBLISHED ONLINE: 3 OCTOBER 2016 | DOI: 10.1038/NPHYS3900
nature physics

Superfluid Brillouin optomechanics

A. D. Kashkanova[1], A. B. Shkarin[1], C. D. Brown[1], N. E. Flowers-Jacobs[1], L. Childress[1,2], S. W. Hoch[1], L. Hohmann[3], K. Ott[3], J. Reichel[3] and J. G. E. Harris[1,4]*

Optomechanical systems couple an electromagnetic cavity to a mechanical resonator which typically is a solid object. The range of phenomena accessible in these systems depends on the properties of the mechanical resonator and on the manner in which it couples to the cavity fields. In both respects, a mechanical resonator formed from superfluid liquid helium offers several appealing features: low electromagnetic absorption, high thermal conductivity, vanishing viscosity, well-understood mechanical loss, and *in situ* alignment with cryogenic cavities. In addition, it offers degrees of freedom that differ qualitatively from those of a solid. Here, we describe an optomechanical system consisting of a miniature optical cavity filled with superfluid helium. The cavity mirrors define optical and mechanical modes with near-perfect overlap, resulting in an optomechanical coupling rate ∼3 kHz. This coupling is used to drive the superfluid and is also used to observe the thermal motion of the superfluid, resolving a mean phonon number as low as eleven.

Light confined in a cavity exerts forces on the components that form the cavity. These forces can excite mechanical vibrations in the cavity components, and these vibrations can alter the propagation of light in the cavity. This interplay between electromagnetic (EM) and mechanical degrees of freedom is the basis of cavity optomechanics. It gives rise to a variety of nonlinear phenomena in both the EM and mechanical domains, and provides means for controlling and sensing EM fields and mechanical oscillators[1].

If the optomechanical interaction is approximately unitary, it can provide access to quantum effects in the optical and mechanical degrees of freedom[1]. Optomechanical systems have been used to observe quantum effects which are remarkable in that they are associated with the motion of massive objects[2–13]. They have also been proposed for use in a range of quantum information and sensing applications[14–21]. Realizing these goals typically requires strong optomechanical coupling, weak EM and mechanical loss, efficient cooling to cryogenic temperatures, and reduced influence from technical noise.

So far, nearly all optomechanical devices have used mechanical oscillators formed by solid objects[1] or clouds of ultracold atomic gases[4,22,23]. However, liquid oscillators offer potential advantages with respect to both solids and ultracold gases. A liquid can conformally fill a hollow EM cavity[24], allowing for near-perfect overlap between the cavity's EM modes and the liquid's normal modes of vibration. Alternatively, an isolated liquid drop may serve as a compact optomechanical device by confining both EM and mechanical excitations in the drop's whispering gallery modes[25,26]. The liquid's composition can be changed *in situ*[27], an important feature for applications in fluidic sensing. However, most liquids face two important obstacles to operation in or near the quantum regime: their viscosity results in strong mechanical damping, and they solidify when cooled to cryogenic temperatures. Liquid helium is exceptional in both respects, as it does not solidify under its own vapour pressure and possesses zero viscosity in its purely superfluid state. In addition, liquid He has low EM loss and high thermal conductivity at cryogenic temperatures.

The mechanical and EM properties of liquid helium are both well-studied[28,29]. The interaction of light with mechanical excitations of superfluid He has also been studied in a variety of contexts, including free-space (that is, without a cavity) spontaneous inelastic light scattering from thermal excitations of first sound, second sound, isotopic concentration, ripplons, and rotons[30–34]. These experiments were carried out at relatively high temperatures ($T \sim 1$–2 K), where these excitations are strongly damped. The combination of strong damping and the lack of confinement for the optical or mechanical modes precluded observation of cavity optomechanical behaviour. More recently, cavity optomechanical interactions were measured between near-infrared (NIR) light in a cavity and the third sound modes of a superfluid He film coating the cavity[35]. This interaction was found to be fairly strong and was used to monitor and control the superfluid's thermal motion; as such it is an important advance in superfluid optomechanics. However, its predominantly non-unitary photothermal origin represents a challenge to studying quantum optomechanical effects[1]. In the microwave domain, a cavity was used to monitor externally driven acoustic (first sound) modes of superfluid He inside the cavity[36]. This device demonstrated very high values of both the acoustic quality factor ($\sim 10^7$) and the EM quality factor ($\sim 10^7$); however, the weak optomechanical coupling (estimated single-photon coupling rate $\sim 4 \times 10^{-8}$ Hz) precluded observation of the superfluid's thermal motion or the cavity field's influence upon the acoustic modes.

Here, we describe an optomechanical system consisting of a NIR optical cavity filled with superfluid He. We observe coupling between the cavity's optical modes and the superfluid's acoustic modes, and find that this coupling is predominantly electrostrictive in origin (and hence unitary). The single-photon coupling rate is $\sim 3 \times 10^3$ Hz, enabling observation of the superfluid's thermal motion and of the cavity field's influence upon the acoustic modes. These modes are cooled to 180 mK (corresponding to mean phonon number 11), and reach a maximum quality factor 6×10^4. These results agree with a simple model based on well-known material properties, and may be improved substantially via straightforward modifications of the present device.

The system is shown schematically in Fig. 1a. The optical cavity is formed between a pair of single-mode optical fibres. Laser machining is used to produce a smooth concave surface on the

[1]Department of Physics, Yale University, New Haven, Connecticut 06511, USA. [2]Department of Physics, McGill University, 3600 Rue University, Montreal, Quebec H3A 2T8, Canada. [3]Laboratoire Kastler Brossel, ENS-PSL Research University, CNRS, UPMC-Sorbonne Universités, Collège de France, F-75005 Paris, France. [4]Department of Applied Physics, Yale University, New Haven, Connecticut 06511, USA. *e-mail: jack.harris@yale.edu

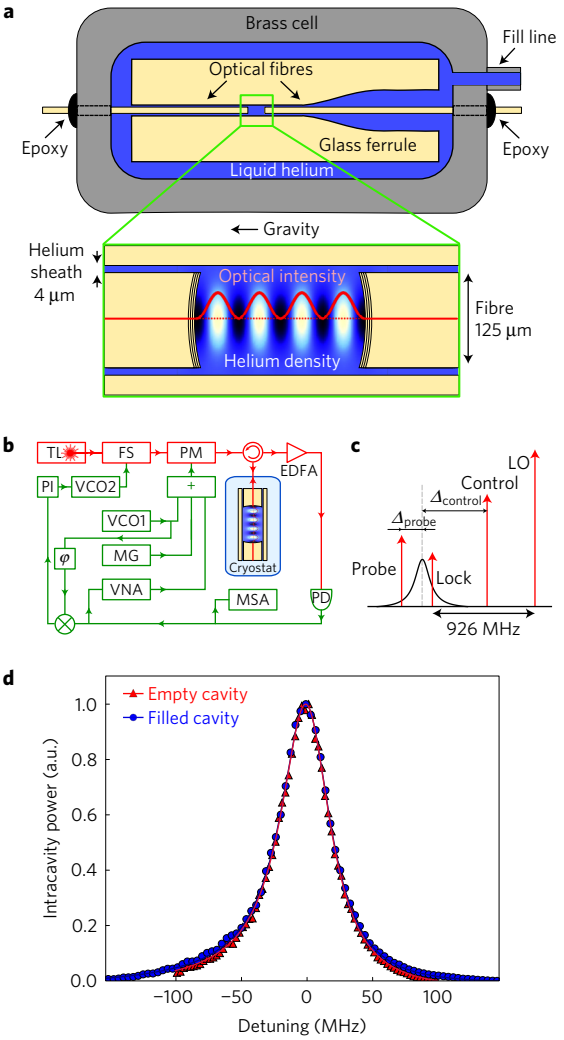

Figure 1 | Description and characterization of the superfluid-filled optical cavity. a, Schematic illustration of the device, showing the optical cavity formed between two optical fibres (yellow) aligned in a glass ferrule (yellow). The ferrule is mounted in a brass cell (grey), which is attached to a dilution refrigerator (not shown) and can be filled with superfluid helium (blue). The lower panel shows an expanded view illustrating the optomechanical coupling: the intensity maxima of an optical mode (red line) overlap with the density maxima of an acoustic mode (blue shading; lighter corresponds to denser He). For clarity, the illustration shows a cavity with length $L = 2\lambda_\alpha$; in the actual device $L \approx 100\lambda_\alpha$. **b**, Schematic of the measurement set-up. Red: optical components. Green: electronic components. Light from a tunable laser (TL) passes through a frequency shifter (FS) and a phase modulator (PM). The PM is driven by tones from a voltage-controlled oscillator (VCO1), microwave generator (MG), and vector network analyser (VNA). The resulting sidebands and the carrier are delivered to the cryostat by a circulator (circle), which also sends the reflected beams through an erbium-doped fibre amplifier (EDFA, triangle) to a photodiode (PD). The photocurrent can be monitored by the VNA or a microwave spectrum analyser (MSA). It is also mixed with the tone from VCO1 to produce an error signal that is sent to VCO2, which in turn drives the FS in order to lock the beams to the cavity. **c**, Illustration of the laser beams. The LO, control, lock, and probe beams are shown (red), along with the cavity lineshape (black). **d**, Intracavity power as the probe beam is detuned. Red: empty cavity. Blue: cavity filled with liquid He. To aid comparison, the data are normalized to their maximum value and plotted as a function of the detuning from the cavity resonance. The solid red and blue lines are fits to the expected Lorentzian, and give linewidths 46.1 ± 0.1 MHz and 46.3 ± 0.2 MHz, respectively.

face of each fibre[37]. The radii of curvature of the two faces are $R_1 = 409\,\mu\text{m}$ and $R_2 = 282\,\mu\text{m}$. On each face, alternating layers of SiO_2 and Ta_2O_5 are deposited to form a distributed Bragg reflector (DBR)[38]. The power transmissions of the DBRs are $T_1 = 1.03 \times 10^{-4}$ and $T_2 = 1.0 \times 10^{-5}$; as a result the cavity is approximately single-sided. The fibres are aligned in a glass ferrule with inner diameter $133 \pm 5\,\mu\text{m}$, as described in ref. 39, and the ferrule is epoxied into a brass cell. The cell is mounted on the mixing chamber (MC) of a dilution refrigerator. Liquid He is introduced into the cell via a fill line. The measurements described here were carried out over two cooldowns; during the first (data in Fig. 1d) the cavity length $L = 67.3\,\mu\text{m}$; during the second (all other data) $L = 85.2\,\mu\text{m}$.

A closer view of the cavity is shown in the lower panel of Fig. 1a. The optical modes are confined by the high reflectivity and concave shape of the DBRs. The acoustic modes are confined in the same manner (the high acoustic reflectivity is primarily due to impedance mismatch between He and the DBR materials, see Supplementary Information). Coupling between the optical and acoustic modes arises via stimulated Brillouin scattering (SBS): the local optical field exerts an electrostrictive force on the liquid, and the liquid's local compression or rarefaction can scatter the light. In regions of the cavity far from the mirrors (that is, where translational symmetry is preserved), conservation of momentum and energy dictate that travelling photons with wavelength λ_α primarily scatter into photons of the same wavelength travelling in the opposite direction by absorbing (emitting) a phonon of wavelength $\lambda_\beta = \lambda_\alpha/2$ moving in the opposite (same) direction[40]. In contrast with many systems exhibiting this 'backwards SBS' process, the acoustic and optical waves in this device are confined in a Fabry–Perot cavity that is much shorter than the optical and acoustic decay lengths (as shown below)[41]. As a result, the acoustic and optical normal modes are standing waves rather than travelling waves, and their coupling may be understood as arising because the spatial variation of He density associated with a standing acoustic mode can alter the effective cavity length for a standing optical mode; equivalently, the intensity variation associated with a standing optical mode can exert an electrostrictive force that drives a standing acoustic mode.

This coupling is described by the conventional optomechanical Hamiltonian[1] $\hat{H}_{\text{OM}} = \hbar g_0^{\alpha,\beta} \hat{a}_\alpha^\dagger \hat{a}_\alpha (\hat{b}_\beta^\dagger + \hat{b}_\beta)$, where $\hat{a}_\alpha^\dagger$ is the photon creation operator for the optical mode α, $\hat{b}_\beta^\dagger$ is the phonon creation operator for the acoustic mode β, and the single-photon coupling rate is

$$g_0^{\alpha,\beta} = \omega_\alpha (n_{\text{He}} - 1) \int \tilde{\rho}_{\beta,\text{zp}} B_\beta(\boldsymbol{r}) \, |\boldsymbol{A}_\alpha(\boldsymbol{r})|^2 \, \mathrm{d}^3\boldsymbol{r} \qquad (1)$$

Here, $\boldsymbol{A}_\alpha(\boldsymbol{r})$ and $B_\beta(\boldsymbol{r})$ are dimensionless, square-normalized functions representing the electric field of the optical mode α and the density variation of the acoustic mode β, respectively. $\tilde{\rho}_{\beta,\text{zp}}$ is the fractional density change associated with the zero-point fluctuations of the acoustic mode β, and is defined by $K_{\text{He}} \int \left(\tilde{\rho}_{\beta,\text{zp}} B_\beta(\boldsymbol{r})\right)^2 \mathrm{d}^3\boldsymbol{r} = \hbar\omega_\beta/2$. The frequency of the optical (acoustic) mode is ω_α (ω_β). The bulk modulus and index of refraction of liquid He are $K_{\text{He}} = 8.21 \times 10^6$ Pa and $n_{\text{He}} = 1.028$, respectively.

The normal modes $\boldsymbol{A}_\alpha(\boldsymbol{r})$ and $B_\beta(\boldsymbol{r})$ can be found by noting that, inside the cavity, Maxwell's equations and the hydrodynamic equations both reduce to wave equations: the former owing to the absence of EM sources, and the latter under the assumption that the liquid undergoes irrotational flow with small velocity, small displacements, and small variations in pressure and density[42]. Furthermore, the cavity geometry (set by R_1, R_2, and L) and the wavelengths of interest (discussed below) allow the paraxial approximation to be used, leading to well-known solutions[43]. As a result, the optical and acoustic modes share the same general form: a standing wave along the cavity axis and a transverse profile described by two Hermite–Gaussian polynomials. Each mode is

indexed by three positive integers, that is: $\alpha = \{x_\alpha, y_\alpha, z_\alpha\}$ and $\beta = \{x_\beta, y_\beta, z_\beta\}$, where the x_α, y_α (x_β, y_β) index the transverse optical (acoustic) mode, and z_α (z_β) is the number of optical (acoustic) half-wavelengths in the cavity. Here, we consider only the lowest-order transverse modes (that is, those with $x_\alpha, y_\alpha, x_\beta, y_\beta = 0$).

Boundary conditions ensure that the interface between the DBR and the liquid He corresponds (nearly) to a node of $\boldsymbol{A}_\alpha$ and an antinode of B_β. As a result, it is straightforward to show that $g_0^{\alpha,\beta}$ nearly vanishes unless $2z_\alpha = z_\beta$ (equivalent to the phase-matching condition for backwards SBS[40] applied to the standing waves of a paraxial cavity). Thus, an optical mode with wavelength (in liquid He) $\lambda_\alpha = 1.50\,\mu\text{m}$ ($\omega_\alpha/2\pi = 194.5\,\text{THz}$) will couple primarily to a single acoustic mode with wavelength $\lambda_\beta = 0.75\,\mu\text{m}$ ($\omega_\beta/2\pi = 317.5\,\text{MHz}$). A derivation of these features from first principles is given in ref. 44.

The measurement set-up is illustrated in Fig. 1b,c. Light from a tunable laser ($1{,}520\,\text{nm} < \lambda < 1{,}560\,\text{nm}$) passes through a frequency shifter (FS) and a phase modulator (PM). The PM is driven by as many as three tones, resulting in first-order sidebands labelled as lock, probe, and control in Fig. 1c, while the carrier beam serves as a local oscillator (LO). Light is delivered to (and collected from) the cryostat via a circulator. Light leaving the cavity passes through an erbium-doped fibre amplifier (EDFA) and then is detected by a photodiode.

The lock beam is produced by a fixed frequency drive ($\omega_{\text{lock}}/2\pi = 926\,\text{MHz}$). The beat note between the reflected lock beam and LO beam produces an error signal that is used to control the FS, ensuring that all the beams track fluctuations in the cavity.

The probe beam is produced by the variable frequency drive (ω_{probe}) from a vector network analyser (VNA). The beat note between the reflected probe and LO beams is monitored by the VNA. The red data in Fig. 1d show the intracavity power inferred from the VNA signal as ω_{probe} is varied to scan the probe beam over the optical mode with $z_\alpha = 90$. These data are taken without He in the cell and with the refrigerator temperature $T_{\text{MC}} = 30\,\text{mK}$. Fitting these data gives the decay rate $\kappa_\alpha/2\pi = (46.1 \pm 0.1)\,\text{MHz}$, typical of the decay rates measured with the cavity at room temperature.

To determine whether the presence of liquid He alters the cavity's optical loss, the blue data in Fig. 1d show the same measurement after the cavity is filled with liquid He. For this measurement, $z_\alpha = 93$ and $T_{\text{MC}} = 38\,\text{mK}$. Fitting these data gives $\kappa_\alpha/2\pi = (46.3 \pm 0.2)\,\text{MHz}$. The difference between the two values of κ_α is consistent with the variations between modes when the cavity is empty, and is also consistent with the negligible optical loss expected for liquid He at these temperatures[45].

The acoustic modes of the liquid He were characterized via optomechanically induced amplification (OMIA)[46]. To accomplish this, a control beam was produced by the variable frequency (ω_{control}) drive from a microwave generator. When the difference $|\omega_{\text{control}} - \omega_{\text{probe}}| \approx \omega_\beta$, the intracavity beating between the control and probe beams can excite the acoustic mode β; the resulting acoustic oscillations modulate the control beam, and these modulations are detected by the VNA (see Supplementary Information).

Figure 2a shows a typical record of the normalized amplitude a and phase ψ of the VNA signal when the control beam is detuned from the cavity resonance by $\Delta_{\text{control}} \approx \omega_\beta$ and ω_{probe} is varied. The peak at $|\omega_{\text{control}} - \omega_{\text{probe}}|/2\pi \approx 317.32\,\text{MHz}$ corresponds to the resonance of the acoustic mode. The solid line in Fig. 2a is a fit to the expected form of a and ψ (see Supplementary Information). The fit parameters are ω_β, γ_β (the acoustic damping rate), as well as A and Ψ (the overall amplitude and phase of the OMIA lineshape, described in Supplementary Information).

Figure 2b shows A and Ψ (extracted from fits similar to the one in Fig. 2a) as a function of Δ_{control} and P_{control} (the power of the control beam). For each P_{control}, A shows a peak of width κ_α centred at $\Delta_{\text{control}} = \omega_\beta$, while Ψ changes by $\sim\pi$ over the same range of Δ_{control}. These features correspond to the excitation of the optical resonance by the probe beam. Fitting the measurements of A and Ψ to the expected form of the OMIA response (assuming purely electrostrictive coupling) gives the dashed lines in Fig. 2b. This fit has only one parameter ($g_0^{\alpha,\beta}$) and returns the best-fit value $g_0^{\alpha,\beta}/2\pi = (3.3 \pm 0.2) \times 10^3\,\text{Hz}$; in comparison, numerical evaluation of equation (1) gives $g_0^{\alpha,\beta}/2\pi = (3.5 \pm 0.5) \times 10^3\,\text{Hz}$.

Although this fit captures many features of the data, it overestimates Ψ by an amount roughly independent of Δ_{control} and P_{control}. To account for this constant phase shift, we calculated the

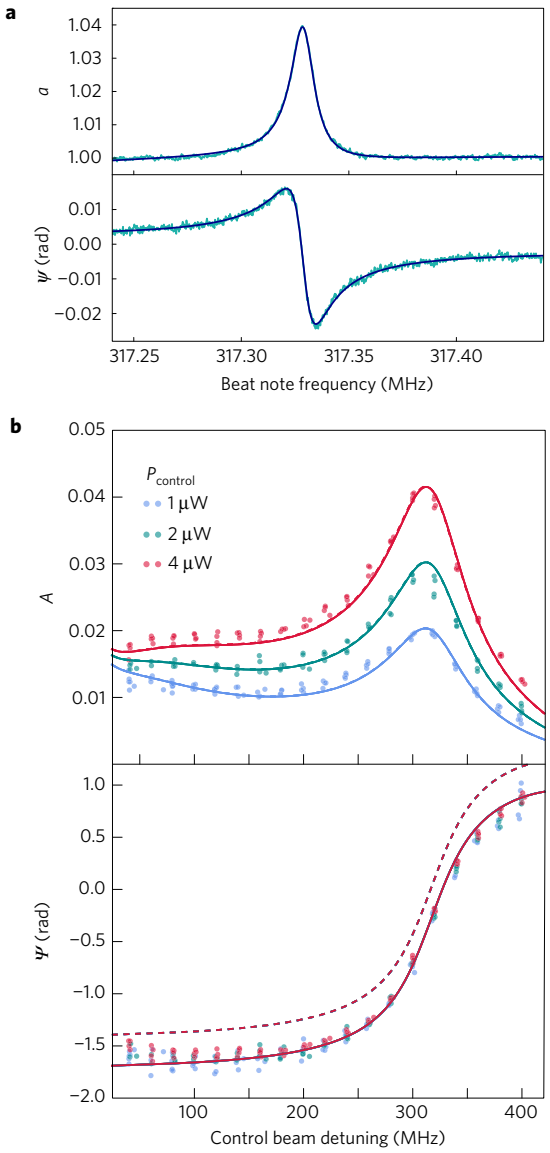

Figure 2 | Characterizing the acoustic mode and the optomechanical coupling. a, Relative amplitude a and phase ψ of the OMIA signal as a function of the intracavity beat note frequency $|\omega_{\text{control}} - \omega_{\text{probe}}|/2\pi$. For these measurements $L = 85.2\,\mu\text{m}$, $z_\alpha = 112$, $z_\beta = 224$, $\kappa_\alpha/2\pi = 69 \pm 2\,\text{MHz}$, $\Delta_{\text{control}}/2\pi = 320\,\text{MHz}$, $P_{\text{control}} = 4\,\mu\text{W}$, and $T_{\text{MC}} = 59\,\text{mK}$. The solid line is the fit described in the text and Supplementary Information. **b**, Amplitude A and phase Ψ of the OMIA lineshape (determined from fits similar to the one in **a**) as a function of Δ_{control} and P_{control}. The dashed line is the fit assuming only electrostrictive coupling; the solid line is the fit assuming electrostrictive and slow photothermal coupling, as described in the text and Supplementary Information (note that the two fits are indistinguishable in the upper panel).

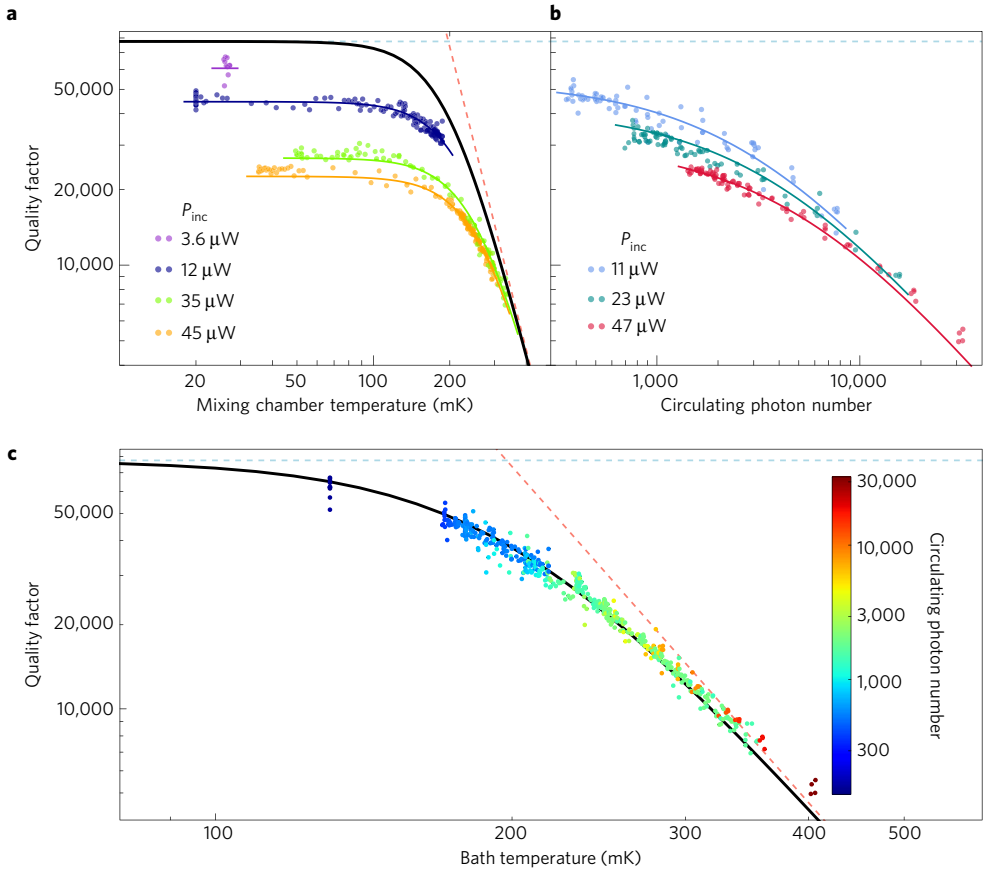

Figure 3 | Acoustic damping as a function of temperature. a, Acoustic quality factor Q_β versus T_{MC}. Different colours correspond to different values of P_{inc}, the total optical power incident on the cavity. The red and blue dashed lines are the predicted contributions to Q_β from the internal loss and radiation loss, respectively, assuming $T_{bath} = T_{MC}$; the solid black line is the net effect of these contributions. The coloured solid lines are the fit to the model described in the text. **b**, Q_β versus $\bar{n}_\alpha$ (the mean intracavity photon number). Different colours correspond to different values of P_{inc}. The coloured solid lines are the fit to the model described in the text. **c**, Data from **a** and **b**, plotted versus T_{bath} (which is inferred from the fits in **a** and **b**). Different colours correspond to different values of $\bar{n}_\alpha$. The solid black line, as well as the dashed red and blue lines, are the same as in **a**.

OMIA signal that would result if the optical intensity also drives the acoustic mode via an interaction mediated by a process much slower than ω_β (see Supplementary Information). Such a slow interaction would arise naturally from a photothermal process in which optical absorption in the DBR heats the liquid He. The solid lines in Fig. 2b are a fit to this calculation, in which the fit parameters are $g_0^{\alpha,\beta}$ and $g_{0,pt}^{\alpha,\beta}$ (the single-photon photothermal coupling rate) and the best-fit values are $g_0^{\alpha,\beta}/2\pi = (3.18 \pm 0.2) \times 10^3$ Hz and $g_{0,pt}^{\alpha,\beta}/2\pi = (0.97 \pm 0.05) \times 10^3$ Hz, respectively.

The damping of the acoustic modes is expected to be dominated by two processes. The first is mode conversion via the nonlinear compressibility of liquid He. This process has been studied extensively[28], and for the relevant temperature range would result in an acoustic quality factor $Q_{\beta,int} = \omega_\beta/\gamma_\beta = \chi/T_{bath}^4$, where $\chi = 118\,K^4$ (see Supplementary Information) and T_{bath} is the temperature of the He in the cavity. The second expected source of damping is acoustic radiation from the He into the confining materials. This process is predicted to result in $Q_{\beta,ext} = (79 \pm 5) \times 10^3$ (see Supplementary Information).

Figure 3a shows Q_β (determined from data and fits similar to Fig. 2a) as a function of T_{MC} and P_{inc} (the total laser power incident on the cavity). Also shown are the predicted $Q_{\beta,int}$ and $Q_{\beta,ext}$ (dashed lines), and their combined effect assuming $T_{bath} = T_{MC}$ (black line). Although the data show qualitative agreement with the predicted trends, there is also a clear dependence of Q_β upon P_{inc}. Figure 3(b) shows that Q_β depends on the mean intracavity photon number $\bar{n}_\alpha$ as well as P_{inc}.

For the conditions of these measurements, dynamical backaction[1] (that is, optical damping) is not expected to contribute appreciably to Q_β. Instead, we consider a model in which light is absorbed in the DBRs, resulting in heat flow into the cavity $\Phi = \mu P_{inc} + \nu\hbar\omega_\alpha\kappa_{\alpha,int}\bar{n}_\alpha$. Here, $\kappa_{\alpha,int}$ is the intracavity loss rate (and is determined from measurements similar to those shown in Fig. 1d), while ν and μ are dimensionless constants that characterize, respectively, the absorbers' overlap with the cavity's optical standing mode (which extends into the upper layers of the DBRs) and the input fibre's optical travelling mode. In the presence of Φ, equilibrium is maintained by the thermal conductance between the cavity and the MC, which is limited by the sheath of liquid He between the optical fibres and the glass ferrule (Fig. 1a). For the relevant temperature range, the conductance of liquid He is $k = \varepsilon T^3$, where T is the local temperature and ε is measured to be $(5 \pm 2.5) \times 10^{-5}\,W\,K^{-4}$ (see Supplementary Information). This model predicts that

$$T_{bath} = \left(T_{MC}^4 + \frac{4}{\varepsilon}(\mu P_{inc} + \nu\hbar\omega_\alpha\kappa_{\alpha,int}\bar{n}_\alpha)\right)^{1/4} \quad (2)$$

The coloured solid lines in Fig. 3a,b are the result of fitting the complete data set to $Q_\beta(T_{bath}) = (Q_{\beta,int}^{-1}(T_{bath}) + Q_{\beta,ext}^{-1})^{-1}$ by using equation (2) and taking ν/μ, μ/ε, and $Q_{\beta,ext}$ as fitting parameters. This fit gives $\nu/\mu = 388 \pm 72$, $\mu/\varepsilon = (12 \pm 2)\,K^4\,W^{-1}$, and $Q_{\beta,ext} = (70 \pm 2.0) \times 10^3$. The value of ν/μ is consistent with absorbers being distributed throughout the DBR layers, and the

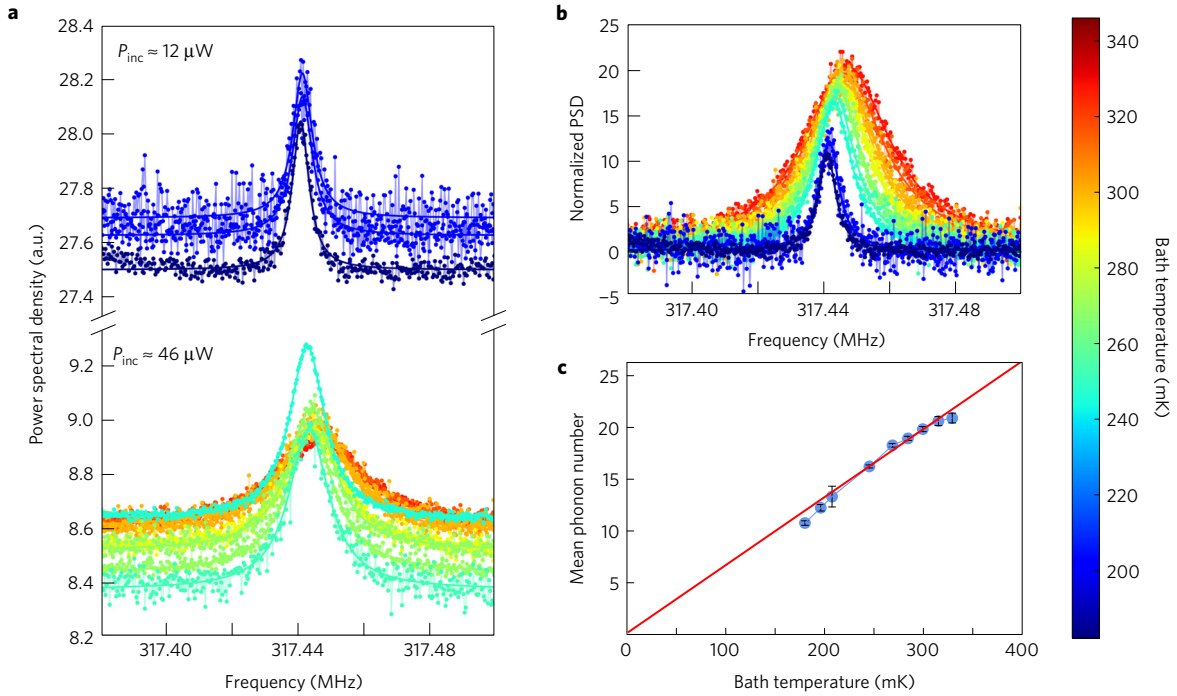

Figure 4 | Thermal fluctuations of the acoustic mode. a, Power spectral density of the photocurrent for various T_{MC} and P_{inc} when no drive is applied to the acoustic mode. The measurement noise floor changes with P_{inc} owing to nonlinearity of the EDFA. The solid lines are fits to a Lorentzian plus a constant background. **b**, Same data as in **a**, converted from photocurrent to helium density fluctuations. The background has been subtracted and the data normalized so that the peak height corresponds to the mean phonon number $\bar{n}_\beta$. **c**, Mean phonon number $\bar{n}_\beta$ versus T_{bath}. Error bars: the standard deviation of multiple measurements of $\bar{n}_\beta$ at each value of T_{bath}.

value of $Q_{\beta,ext}$ is consistent with the a priori calculation in the Supplementary Information.

Figure 3c shows the data from Fig. 3a,b replotted as a function of T_{bath} (calculated from equation (2) and the best-fit values of ν/μ and μ/ε). The data collapse together, indicating that Q_β is determined by T_{bath}, which in turn is determined by T_{MC}, P_{inc} and $\bar{n}_\alpha$ in accordance with the model described above. The collapsed data are in close agreement with the prediction for $Q_\beta(T_{bath})$ (the black line in Fig. 3c).

To determine $\bar{n}_\beta$ (the mean phonon number of the acoustic mode), a heterodyne technique was used to measure the Stokes sideband imprinted on the control beam by the acoustic mode's thermal fluctuations. For these measurements, the probe beam was turned off and the control beam's detuning relative to the cavity resonance was set to $\Delta_{control} \approx \omega_\beta$. A spectrum analyser was used to monitor the photocurrent at frequencies near the beat note between the Stokes sideband and the LO. Figure 4a shows $S_{II}(\omega)$, the power spectral density (PSD) of the photocurrent, for a range of T_{MC} and P_{inc}. As T_{MC} and P_{inc} are reduced the acoustic resonances become narrower, in qualitative agreement with Fig. 3.

Figure 4b shows the same data as in Fig. 4a, but with S_{II} converted to $S_{\tilde{\rho}\tilde{\rho}}$ (the PSD of fractional density fluctuations), and normalized by $4\tilde{\rho}^2_{\beta,zp}/\gamma_\beta$ (see Supplemental Information) so that the peak height corresponds to $\bar{n}_\beta$. The solid lines are fits to the expected Lorentzian lineshape. Figure 4c shows $\bar{n}_\beta$ determined from these fits and plotted as a function of T_{bath} (determined using equation (2)). Also shown is the solid red line corresponding to the prediction $\bar{n}_\beta = k_B T_{bath}/\hbar\omega_\beta$. The data and prediction show close agreement for $\bar{n}_\beta$ as low as 11 ± 0.3, indicating that the acoustic mode remains in thermal equilibrium with the material temperature T_{bath}.

In conclusion, these results demonstrate a promising combination of cavity optomechanics with a superfluid liquid. This system requires no *in situ* alignment, and achieves dimensionless figures of merit comparable to state-of-the-art optomechanical systems, for example, in sideband resolution ($\omega_\beta/\kappa_\alpha = 4.6$), bath phonon occupancy ($\bar{n}_{bath} \equiv k_B T_{bath}/\hbar\omega_\beta = 11$), and single-photon cooperativity ($C_0 = 4(g_0^{\alpha,\beta})^2/\kappa_\alpha\gamma_\beta = 1.5 \times 10^{-4}$). The maximum multi-photon cooperativity ($C = 0.03$) is relatively modest, as $\bar{n}_\alpha$ is limited by heating from optical absorption in the mirrors. Some quantum optomechanical phenomena (such as quantum asymmetry and correlation in the motional sidebands) may be observed in devices with these parameters[47]; other goals, such as ground-state cooling and the production of squeezed or entangled states, typically require $C > 1$ or $C > n_{th}$.

To assess the feasibility of improving C, we note that the simple model which accurately describes the system's performance shows that this performance is not limited by the liquid helium, but rather by the cavity mirrors. Specifically, γ_β is dominated by the mirrors' acoustic transmission, and T_{bath} is dominated by the mirrors' optical absorption. Since T_{bath} also contributes to γ_β (red dashed line in Fig. 3c), substantial improvements will require reducing both the acoustic transmission and the heating due to the optical absorption. As described in the Supplementary Information, the same model that reproduces the data shown here indicates that both of these improvements can be achieved by straightforward refinements. Specifically, γ_β may be decreased by a factor ~40 using DBRs that serve as high-reflectivity acoustic mirrors as well as optical mirrors. In addition, T_{bath} can be lowered by increasing the thermal conductance between the cavity and the refrigerator (for example, using the cavity geometry described in ref. 39). Together, these refinements should lead to $1 < C \approx n_{th}$ (see Supplementary Information).

These results open a number of qualitatively new directions, such as cavity optomechanical coupling to degrees of freedom that are unique to superfluid liquid He, including: the Kelvin modes of remnant vortex lines; ripplon modes of the superfluid's free surface; and well-controlled impurities, such as electrons on the surface or in the bulk of the superfluid. Precision measurements of these degrees

of freedom may provide new insight into long-standing questions about their roles in superfluid turbulence[48,49] and their potential applications in quantum information processing[50].

Data availability. The data that support the plots within this paper and other findings of this study are available from the corresponding author upon reasonable request.

Received 16 February 2016; accepted 20 August 2016; published online 3 October 2016

References

1. Aspelmeyer, M., Marquardt, F. & Kippenberg, T. J. Cavity optomechanics. *Rev. Mod. Phys.* **86,** 1391–1452 (2014).
2. O'Connell, *et al*. Quantum ground state and single-phonon control of a mechanical resonator. *Nature* **464,** 697–703 (2010).
3. Jasper, C. *et al*. Laser cooling of a nanomechanical oscillator into its quantum ground state. *Nature* **478,** 98–92 (2011).
4. Brahms, N., Botter, T., Schreppler, A., Brooks, D. W. C. & Stamper-Kurn, D. M. Optically detecting the quantization of collective atomic motion. *Phys. Rev. Lett.* **108,** 133601 (2012).
5. Safavi-Naeini, A. H. *et al*. Squeezed light from a silicon micromechanical resonator. *Nature* **500,** 185–189 (2013).
6. Palomaki, T. A., Teufel, J. D., Simmonds, R. W. & Lehnert, K. W. Entangling mechanical motion with microwave fields. *Science* **342,** 710–713 (2013).
7. Purdy, T. P., Peterson, R. W. & Regal, C. A. Observation of radiation pressure shot noise on a macroscopic object. *Science* **339,** 801–804 (2013).
8. Meenehan, S. M. *et al*. Pulsed excitation dynamics of an optomechanical crystal resonator near its quantum ground-state of motion. *Phys. Rev. X* **5,** 041002 (2015).
9. Wollmann, E. E. *et al*. Quantum squeezing of motion in a mechanical resonator. *Science* **349,** 952–955 (2015).
10. Pirkkalainen, J.-M., Damskägg, E., Brandt, M., Massel, F. & Sillanpää, M. A. Squeezing of quantum noise of motion in a micromechanical resonator. *Phys. Rev. Lett.* **115,** 243601 (2015).
11. Purdy, T. P. *et al*. Optomechanical Raman-ratio thermometry. *Phys. Rev. A* **92,** 031802(R) (2015).
12. Underwood, M. *et al*. Measurement of the motional sidebands of a nanogram-scale oscillator in the quantum regime. *Phys. Rev. A* **92,** 061801(R) (2015).
13. Reidinger, R. *et al*. Non-classical correlations between single photons and phonons from a mechanical oscillator. *Nature* **530,** 313–316 (2016).
14. Ma, Y. *et al*. Narrowing the filter-cavity bandwidth in gravitational-wave detectors via optomechanical interaction. *Phys. Rev. Lett.* **113,** 151102 (2014).
15. Safavi-Naeini, A. H. & Painter, O. J. Proposal for an optomechanical traveling wave phonon–photon translator. *New J. Phys.* **13,** 013017 (2011).
16. Regal, C. A. & Lehnert, K. W. From cavity electromechanics to cavity optomechanics. *J. Phys. Conf. Ser.* **264,** 012025 (2011).
17. Romero-Isart, O. Quantum superposition of massive objects and collapse models. *Phys. Rev. A* **84,** 052121 (2011).
18. Yang, H. *et al*. Macroscopic quantum mechanics in a classical spacetime. *Phys. Rev. Lett.* **110,** 170401 (2013).
19. Hammerer, K. *et al*. Strong coupling of a mechanical oscillator and a single atom. *Phys. Rev. Lett.* **103,** 063005 (2009).
20. Hammerer, K., Aspelmeyer, M., Polzik, E. S. & Zoller, P. Establishing Einstein–Podolsky–Rosen channels between nanomechanics and atomic ensembles. *Phys. Rev. Lett.* **102,** 020501 (2009).
21. Rabl, P. *et al*. A quantum spin transducer based on nanoelectromechanical resonator arrays. *Nat. Phys.* **6,** 602–608 (2010).
22. Gupta, S., Moore, K. L., Murch, K. W. & Stamper-Kurn, D. M. Cavity nonlinear optics at low photon numbers from collective atomic motion. *Phys. Rev. Lett.* **99,** 213601 (2007).
23. Brennecke, F., Ritter, S., Donner, T. & Esslinger, T. Cavity optomechanics with a Bose–Einstein condensate. *Science* **322,** 235–238 (2008).
24. Colgate, S. O., Sivaraman, A., Dejsupa, C. & McGill, K. C. Acoustic cavity method for phase boundary determinations: the critical temperature of CO_2. *Rev. Sci. Instr.* **62,** 198–202 (1991).
25. Tzeng, H. M., Long, M. B., Chang, R. K. & Barber, P. W. Laser-induced shape distortions of flowing droplets deduced from morphology-dependent resonances in fluorescent spectra. *Opt. Lett.* **10,** 209–211 (1985).
26. Dahan, R., Martin, L. L. & Carmon, T. Droplet optomechanics. *Optica* **3,** 175–178 (2016).
27. Bahl, G. *et al*. Brillouin cavity optomechanics with microfluidic devices. *Nat. Commun.* **4,** 1994 (2013).
28. Maris, H. J. Phonon–phonon interactions in liquid helium. *Rev. Mod. Phys.* **49,** 341–359 (1977).
29. Donnelly, R. J. & Barenghi, C. F. The observed properties of liquid helium at the saturated vapor pressure. *J. Phys. Chem. Ref. Data* **27,** 1217–1274 (1998).
30. Greytak, T. J. & Yan, J. Light scattering from rotons in liquid helium. *Phys. Rev. Lett.* **22,** 987–990 (1969).
31. Greytak, T. J., Woerner, R., Yan, J. & Benjamin, R. Experimental evidence for a two-proton bound state in superfluid helium. *Phys. Rev. Lett.* **25,** 1547–1550 (1970).
32. Palin, C. J., Vinen, W. F., Pike, E. R. & Vaughan, J. M. Rayleigh and Brillouin scattering from superfluid ^{3}He-^{4}He mixtures. *J. Phys. C* **4,** L225–L228 (1971).
33. Wagner, F. Scattering of light by thermal ripplons on superfluid helium. *J. Low Temp. Phys.* **13,** 317–330 (1973).
34. Rockwell, D. A., Benjamin, R. F. & Greytak, T. J. Brillouin scattering from superfluid ^{3}He-^{4}He solutions. *J. Low Temp. Phys.* **18,** 389–425 (1975).
35. Harris, G. I. *et al*. Laser cooling and control of excitations in superfluid helium. *Nat. Phys.* **12,** 788–793 (2016).
36. DeLorenzo, L. A. & Schwab, K. C. Superfluid optomechanics: coupling of a superfluid to a superconducting condensate. *New J. Phys.* **16,** 113020 (2014).
37. Hunger, D., Deutsch, C., Barbour, R. J., Warburton, R. J. & Reichel, J. Laser fabrication of concave, low-roughness features in silica. *AIP Adv.* **2,** 012119 (2012).
38. Rempe, G., Thompson, R. J., Kimble, H. J. & Lalezari, R. Measurement of ultralow losses in an optical interferometer. *Opt. Lett.* **17,** 363–365 (1992).
39. Flowers-Jacobs, N. E. *et al*. Fiber-cavity-based optomechanical device. *Appl. Phys. Lett.* **101,** 221109 (2012).
40. Damzen, M. J., Vlad, V. I., Babin, V. & Mocofanescu, A. *Stimulated Brillouin Scattering* (Taylor & Francis, 2003).
41. Van Laer, R., Baets, R. & Van Thourhout, D. Unifying Brillouin scattering and cavity optoechanics. *Phys. Rev. A* **93,** 053828 (2016).
42. Bohr, A. & Mottelson, B. R. *Nuclear Structure* (World Scientific, 1997).
43. Siegman, A. E. *Lasers* (University Science Books, 1986).
44. Agarwal, G. S. & Jha, S. S. Theory of optomechanical interactions in superfluid He. *Phys. Rev. A* **90,** 023812 (2014).
45. Seidel, G. M., Lanou, R. E. & Yao, W. Rayleigh scattering in rare-gas liquids. *Nuc. Instr. Meth. Phys. Res. A* **489,** 189–194 (2002).
46. Weis, S. *et al*. Optomechanically induced transparency. *Science* **330,** 1520–1523 (2010).
47. Purdy, T. P., Grutter, K. E., Srinivasan, K. & Taylor, J. M. Observation of optomechanical quantum correlations at room temperature. Preprint at http://arXiv.org/abs/1605.05664 (2016).
48. Vinen, W. F., Tsubota, M. & Mitani, A. Kelvin-wave cascade on a vortex in superfluid ^{4}He at a very low temperature. *Phys. Rev. Lett.* **91,** 135301 (2003).
49. Kozik, E. & Svistunov, B. Kelvin-wave cascade and decay of superfluid turbulence. *Phys. Rev. Lett.* **92,** 035301 (2004).
50. Platzman, P. M. & Dykman, M. I. Quantum computing with electrons floating on liquid helium. *Science* **284,** 1967–1969 (1999).

Acknowledgements

We are grateful to V. Bernardo, J. Chadwick, J. Cummings, A. Fragner, K. Lawrence, D. Lee, D. McKinsey, P. Rakich, R. Schoelkopf, H. Tang, J. Thompson and Z. Zhao for their assistance. We acknowledge financial support from W. M. Keck Foundation Grant No. DT121914, AFOSR Grants FA9550-09-1-0484 and FA9550-15-1-0270, DARPA Grant W911NF-14-1-0354, ARO Grant W911NF-13-1-0104, and NSF Grant 1205861. This work has been supported by the DARPA/MTO ORCHID Program through a grant from AFOSR. This project was made possible through the support of a grant from the John Templeton Foundation. The opinions expressed in this publication are those of the authors and do not necessarily reflect the views of the John Templeton Foundation. This material is based upon work supported by the National Science Foundation Graduate Research Fellowship under Grant No. DGE-1122492. L.H., K.O. and J.R. acknowledge funding from the EU Information and Communication Technologies Program (QIBEC project, GA 284584), ERC (EQUEMI project, GA 671133), and IFRAF.

Author contributions

A.D.K., A.B.S. and C.D.B. performed the measurements and analysis; A.D.K., A.B.S. and N.E.F.-J. assembled the device; A.D.K. and L.C. built and tested prototypes of the device; S.W.H., L.H. and K.O. carried out the laser machining of the fibres; J.R. supervised the laser machining; J.G.E.H. supervised the other phases of the project.

Additional information

Supplementary information is available in the online version of the paper. Reprints and permissions information is available online at www.nature.com/reprints. Correspondence and requests for materials should be addressed to J.G.E.H.

Competing financial interests

The authors declare no competing financial interests.